Jizhou Song[1]
Department of Mechanical and Aerospace Engineering,
University of Miami,
Coral Gables, FL 33146
e-mail: j.song8@miami.edu

Chaofeng Lu
Department of Civil Engineering and
Soft Matter Research Center,
Zhejiang University,
Hangzhou 310058, China

Xu Xie
Department of Materials Science and Engineering,
Frederick Seitz Materials Research Laboratory,
University of Illinois at Urbana-Champaign,
Urbana, IL 61801

Yuhang Li

Yihui Zhang

Department of Civil and Environmental Engineering,
Department of Mechanical Engineering,
Northwestern University,
Evanston, IL 60208

Kyle L. Grosse
Department of Mechanical Science and Engineering,
University of Illinois at Urbana-Champaign,
Urbana, IL 61801

Simon Dunham
Department of Materials Science and Engineering,
Frederick Seitz Materials Research Laboratory,
University of Illinois at Urbana-Champaign,
Urbana, IL 61801

Yonggang Huang
Department of Civil and Environmental Engineering,
Department of Mechanical Engineering,
Northwestern University,
Evanston, IL 60208

William P. King
Department of Mechanical Science and Engineering,
University of Illinois at Urbana-Champaign,
Urbana, IL 61801

John A. Rogers
Department of Materials Science and Engineering,
Frederick Seitz Materials Research Laboratory,
Department of Mechanical Science and Engineering,
University of Illinois at Urbana-Champaign,
Urbana, IL 61801

Thermomechanical Modeling of Scanning Joule Expansion Microscopy Imaging of Single-Walled Carbon Nanotube Devices

An analytical model, validated by experiments and finite element simulations, is developed to study the thermal imaging of single-walled carbon nanotube (SWNT) devices by scanning Joule expansion microscopy (SJEM). A simple scaling law for thermal expansion at low frequencies, which only depends on two nondimensional geometric parameters, is established. Such a scaling law provides a simple way to determine the surface temperature distribution and power dissipation per unit length in an SWNT from the measured thermal expansion in experiments. The results suggest the spatial resolution of the SJEM measurement is as good as ~50 nm. [DOI: 10.1115/1.4024175]

Keywords: single-walled carbon nanotube, scanning Joule expansion microscopy, thermal expansion

1 Introduction

Single-walled carbon nanotubes (SWNTs) possess superior electrical and thermal properties, which enable high-performance transistors [1,2], advanced interconnects [3], and other components of relevance to various forms of electronics. Joule heating of SWNTs and subsequent thermal transport into the surroundings may critically affect the design, operation, and reliability of SWNT devices. There exist several different approaches to measure the temperature distributions in SWNT devices for understanding the fundamental properties in device design. One such method is known as scanning thermal microscopy (SThM) based on atomic force microscopy (AFM). In SThM, thermocouples or other temperature sensors are fabricated on the very end of AFM cantilever tips to scan over a surface in order to measure the temperature [4–8]. The spatial and temperature resolution of a SThM is limited by the sensor size on a submicrometer scale. Much effort has been focused on reducing the sensor size to increase the resolution at the cost of fabrication difficulty. In addition, the

[1]Corresponding author.
Contributed by the Applied Mechanics Division of ASME for publication in the JOURNAL OF APPLIED MECHANICS. Manuscript received January 16, 2013; final manuscript received February 24, 2013; accepted manuscript posted April 10, 2013; published online May 31, 2013. Assoc. Editor: Huajian Gao.

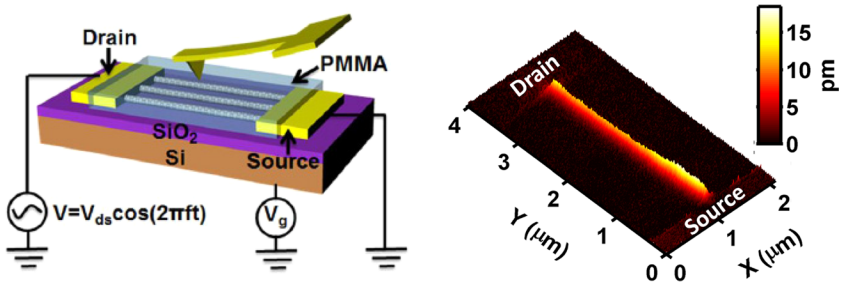

(a) (b)

Fig. 1 (*a*) Schematic illustration of the experimental setup for scanning Joule expansion microscopy imaging of an SWNT device, and (*b*) the SJEM image of an SWNT device collected at $V_{ds} = 4$ V, $f = 30$ kHz and a PMMA thickness ~25 nm

heat flow between the cantilever and substrate can be difficult to accurately describe. To overcome these difficulties, a new technique called scanning Joule expansion microscopy (SJEM) was proposed [9,10]. In SJEM, a conventional AFM cantilever is used to measure the thermal expansion to reveal the underlying temperature distributions.

Xu et al. investigated heat generation and transport in transistors that incorporate straight horizontally aligned arrays of individual SWNTs by SJEM [11]. Several electronic behaviors have been revealed, including metallic and semiconducting responses, spatial variations in diameter or chirality, and localized defect sites. Figure 1(*a*) shows the schematic illustration of the experimental setup for the SJEM measurement of an SWNT device consisting of several SWNTs on an SiO_2/Si substrate. A layer of poly(methyl methacrylate) (PMMA) is coated on the top of the device to protect the SWNTs and amplify the thermomechanical expansion caused by Joule heating of the SWNTs from an alternating voltage $V(t) = V_{ds}\cos(\omega t)$ (with angular frequency ω and frequency $f = \omega/2\pi$) between the drain and source contacts. The resulting time-oscillating temperature increase and thermal expansion will oscillate with frequency $2f$. An AFM probe operating in contact mode is then used to scan the top surface of the PMMA and measure the vertical displacements. Detection with a lock-in amplifier tuned to frequency $2f$ gives the deflections of the AFM cantilever due to electrically driven thermal expansion, as shown in Fig. 1(*b*). Instead of a numerical modeling of the SJEM [12,13], an analytical thermomechanical model is needed to derive the temperature distributions and power dissipation in an SWNT from measurements of thermal expansion.

The objective of this paper is to develop an analytical thermomechanical model for the SJEM measurement of SWNT devices. A scaling law of thermal expansion at low frequencies is established in terms of nondimensional combinations of material, geometric parameters, and frequency. The analytical model will be validated by the finite element analysis and experiments. The paper is outlined as follows. The thermal modeling for temperature distribution is developed in Sec. 2, while the thermomechanical modeling for thermal expansion is presented in Sec. 3. The scaling law of thermal expansion at low frequencies is given in Sec. 4. The results and discussion are given in Sec. 5.

2 Thermal Modeling for Temperature Distribution

As shown in Fig. 1(*b*), a two dimensional (2D) analysis is reasonable for locations away from the SWNT ends due to the large aspect ratio of SWNTs. The analytically modeled system includes SWNTs on an SiO_2/Si substrate with a PMMA layer on the top, as shown in Fig. 2. Because the thickness of Si, ~500 μm, is much larger than those of SiO_2 ($h_1 \sim 100$nm) and PMMA ($h_0 \sim 100$nm), it is modeled as a semi-infinite substrate. Heat transfer mainly occurs through the surface of SWNTs and, therefore, it can be modeled as a planar heat source at the PMMA-SiO_2 interface. For an SWNT with radius r, the half width of heat source can be approximated by $b = \pi r/2$, such that it has the same circumference. For an applied voltage $V(t) = V_{ds}\cos(\omega t)$, the power dissipation per unit length along the SWNT takes the form of $Q_0[1 + \cos(2\omega t)]$, where Q_0 is the steady-state component and $Q_0\cos(2\omega t)$ is the time-oscillating component. The resulting temperature increase and thermal expansion will have both steady-state and time-oscillating terms. Since the SJEM measures the time-oscillating component of the thermal expansion, we only consider the temperature increase and thermal expansion due to the time-oscillating power dissipation per unit length $Q(t) = Q_0\cos(2\omega t)$.

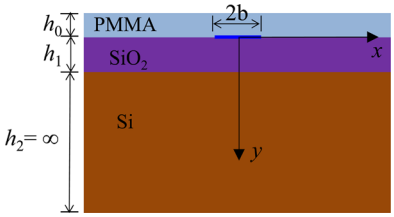

Fig. 2 Schematic illustration of the analytically modeled system

The origin of the coordinate system (x, y) is located at the center of the SWNT, with x along the interface and y pointing into the Si substrate (see Fig. 2). The temperature increase from the ambient temperature $\Delta T(x, y, t) = T - T_\infty$ satisfies the heat conduction equation

$$\frac{\partial \Delta T}{\partial t} - \alpha\left(\frac{\partial^2 \Delta T}{\partial x^2} + \frac{\partial^2 \Delta T}{\partial y^2}\right) = 0 \tag{1}$$

where $\alpha = k/(c\rho)$ is the thermal diffusivity with k as the thermal conductivity, c as the specific heat capacity, and ρ as the mass density. In the following, the subscripts 0, 1, and 2 denote PMMA, SiO_2, and Si, respectively.

A finite element analysis (FEA) shows that the heat losses from radiation and convection are negligible. The top surface of the PMMA ($y = -h_0$) can be assumed to be thermal insulating, which gives

$$-k_0 \left.\frac{\partial \Delta T}{\partial y}\right|_{y=-h_0} = 0 \tag{2}$$

The temperature is continuous across the PMMA-SiO_2 interface ($y = 0$), i.e.,

$$\Delta T|_{y=0^+} = \Delta T|_{y=0^-} \tag{3}$$

and the heat flux is also continuous except for the region of heat source ($y = 0, |x| \le b$)

$$-k_1 \left.\frac{\partial \Delta T}{\partial y}\right|_{y=0^+} + k_0 \left.\frac{\partial \Delta T}{\partial y}\right|_{y=0^-} = \begin{cases} 0 & |x| > b \\ \dfrac{Q(t)}{2b} & |x| \le b \end{cases} \tag{4}$$

Continuity of the temperature and heat flux across the SiO_2-Si interface ($y = h_1$) requires

$$\Delta T|_{y=h_1^+} = \Delta T|_{y=h_1^-} \tag{5}$$

and

$$-k_2 \left.\frac{\partial \Delta T}{\partial y}\right|_{y=h_1^+} = -k_1 \left.\frac{\partial \Delta T}{\partial y}\right|_{y=h_1^-} \tag{6}$$

The ambient temperature at the bottom surface of Si ($y = \infty$) gives

$$\Delta T|_{y=\infty} = 0 \tag{7}$$

The power dissipation per unit length $Q(t) = Q_0 \cos(2\omega t)$ can be written as the real part of $Q_0 e^{i2\omega t}$. The temperature increase has the same frequency and takes the form $\theta(x,y)e^{i2\omega t}$, where $\theta(x,y) = |\theta(x,y)|e^{2i\beta}$ with β as the phase angle of $\theta(x,y)$. The amplitude of the temperature increase is given by $|\theta(x,y)|$. Substitution of $\theta(r,x)e^{i2\omega t}$ into Eq. (1) gives

$$\frac{\partial^2 \theta}{\partial x^2} + \frac{\partial^2 \theta}{\partial y^2} - iq^2\theta = 0 \tag{8}$$

where $q = \sqrt{2\omega/\alpha}$. Due to the symmetry of the problem, we only focus on the region with $x \ge 0$. The Fourier transform

$$\bar{\theta}(s,y) = \sqrt{\frac{2}{\pi}} \int_0^\infty \theta(x,y)\cos(sx)dx$$

of Eq. (8) gives an ordinary differential equation

$$\frac{d^2\bar{\theta}}{dy^2} - (s^2 + iq^2)\bar{\theta} = 0 \tag{9}$$

The preceding equation has the solution

$$\bar{\theta}(s,y) = A(s)e^{y\sqrt{s^2+iq^2}} + B(s)e^{-y\sqrt{s^2+iq^2}} \tag{10}$$

where $A(s)$ and $B(s)$ are to be determined and are denoted by A_0 and B_0 for the PMMA, A_1 and B_1 for SiO_2, and A_2 and B_2 for the PMMA, respectively. The Fourier transform of the boundary and continuity conditions in Eqs. (2)–(6) yield

$$A_0 e^{-h_0\sqrt{s^2+iq_0^2}} - B_0 e^{h_0\sqrt{s^2+iq_0^2}} = 0 \tag{11}$$

$$A_0 + B_0 = A_1 + B_1 \tag{12}$$

$$k_0\sqrt{s^2+iq_0^2}(A_0 - B_0) - k_1\sqrt{s^2+iq_1^2}(A_1 - B_1) = \frac{Q_0 \sin(sb)}{\sqrt{2\pi}bs} \tag{13}$$

$$A_1 e^{h_1\sqrt{s^2+iq_1^2}} + B_1 e^{-h_1\sqrt{s^2+iq_1^2}} = A_2 e^{h_1\sqrt{s^2+iq_2^2}} + B_2 e^{-h_1\sqrt{s^2+iq_2^2}} \tag{14}$$

$$k_1\sqrt{s^2+iq_1^2}\left(A_1 e^{h_1\sqrt{s^2+iq_1^2}} - B_1 e^{-h_1\sqrt{s^2+iq_1^2}}\right) = k_2\sqrt{s^2+iq_2^2}\left(A_2 e^{h_1\sqrt{s^2+iq_2^2}} - B_2 e^{-h_1\sqrt{s^2+iq_2^2}}\right) \tag{15}$$

$$A_2 = 0 \tag{16}$$

Solving Eqs. (11)–(16) yields

$$\begin{Bmatrix} A_0 \\ B_0 \\ A_1 \\ B_1 \\ A_2 \\ B_2 \end{Bmatrix} = \frac{Q_0 \sin\left(\frac{\pi r}{2}s\right)}{\pi r s\sqrt{2\pi}} f(s) \begin{Bmatrix} (1+\kappa)e^{h_0\sqrt{s^2+iq_0^2}} \\ (1+\kappa)e^{-h_0\sqrt{s^2+iq_0^2}} \\ 2\kappa\cosh\left(h_0\sqrt{s^2+iq_0^2}\right) \\ 2\cosh\left(h_0\sqrt{s^2+iq_0^2}\right) \\ 0 \\ 2\cosh\left(h_0\sqrt{s^2+iq_0^2}\right)e^{h_1\sqrt{s^2+iq_2^2}}\left[\kappa e^{h_1\sqrt{s^2+iq_1^2}} + e^{-h_1\sqrt{s^2+iq_1^2}}\right] \end{Bmatrix} \tag{17}$$

where

$$f(s) = \frac{1}{(1-\kappa)k_1\sqrt{s^2+iq_1^2}\cosh\left(h_0\sqrt{s^2+iq_0^2}\right) + (1+\kappa)k_0\sqrt{s^2+iq_0^2}\sinh\left(h_0\sqrt{s^2+iq_0^2}\right)}$$

$$\kappa = \frac{1 - \dfrac{k_2}{k_1}\dfrac{\sqrt{s^2+iq_2^2}}{\sqrt{s^2+iq_1^2}}}{1 + \dfrac{k_2}{k_1}\dfrac{\sqrt{s^2+iq_2^2}}{\sqrt{s^2+iq_1^2}}} e^{-2h_1\sqrt{s^2+iq_1^2}}$$

where $q_0 = \sqrt{2\omega/\alpha_0}$, $q_1 = \sqrt{2\omega/\alpha_1}$, and $q_2 = \sqrt{2\omega/\alpha_2}$.

The inverse Fourier transform

$$\theta(x,y) = \sqrt{\frac{2}{\pi}} \int_0^\infty \bar{\theta}(s,y)\cos(sx)ds$$

gives the temperature increase in the PMMA, SiO_2, and Si as

$$\theta_0(x,y)=\frac{2Q_0}{\pi^2 r}\int_0^\infty \frac{\sin\left(\frac{\pi r}{2}s\right)}{s}f(s)(1+\kappa)\cosh\left[(h_0+y)\sqrt{s^2+iq_0^2}\right]\times\cos(sx)ds$$

$$\theta_1(x,y)=\frac{2Q_0}{\pi^2 r}\int_0^\infty \frac{\sin\left(\frac{\pi r}{2}s\right)}{s}f(s)\cosh\left(h_0\sqrt{s^2+iq_0^2}\right)\times\left(\kappa e^{y\sqrt{s^2+iq_1^2}}+e^{-y\sqrt{s^2+iq_1^2}}\right)\cos(sx)ds$$

$$\theta_2(x,y)=\frac{2Q_0}{\pi^2 r}\int_0^\infty \frac{\sin\left(\frac{\pi r}{2}s\right)}{s}f(s)\cosh\left(h_0\sqrt{s^2+iq_0^2}\right)\times\left(\kappa e^{h_1\sqrt{s^2+iq_1^2}}+e^{-h_1\sqrt{s^2+iq_1^2}}\right)e^{(h_1-y)\sqrt{s^2+iq_2^2}}\cos(sx)ds \tag{18}$$

The temperature increase on the surface ($y=-h_0$) of the PMMA, which is used to compare the FEA in Sec. 5, is given by

$$\theta_{\text{surface}}(x)=\frac{2Q_0}{\pi^2 r}\int_0^\infty \frac{\sin\left(\frac{\pi r}{2}s\right)}{s}f(s)(1+\kappa)\cos(sx)ds \tag{19}$$

and its amplitude is $|\theta_{\text{surface}}(x)|$.

3 Thermomechanical Modeling for Thermal Expansion

The coefficients of thermal expansion (CTEs) of the SiO_2 and Si ($\sim 10^{-6}$) [14,15] are much smaller than that of the PMMA ($\sim 5\times10^{-5}$) [16] and the temperature rise in Si is significant only near its surface and quickly diminishes. [11]. Therefore, the contributions of SiO_2 and Si to the SJEM signal can be neglected. This allows an analytical study of the SJEM signal by only considering thermal expansion in the PMMA layer that is traction-free on the top surface ($y=-h_0$) and fully constrained at the bottom ($y=0$). The problem can be solved by superposing the solutions of two auxiliary problems (see Fig. 3):

(I) an infinite plane with a temperature distribution $\theta_0(x,y)$ obtained in Sec. 2
(II) a finite plane without a temperature distribution but with its upper boundary tractions and lower boundary displacements to negate those from Problem I at the same locations

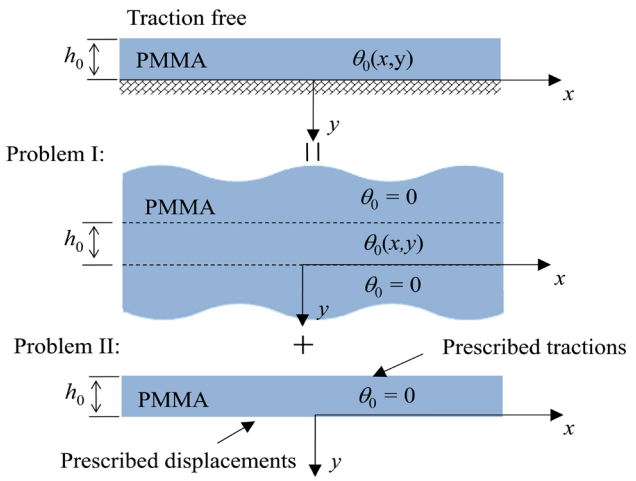

Fig. 3 Schematic illustration of the thermomechanical model

3.1 Solutions for Auxiliary Problem I. Problem I can be solved by introducing a potential of thermal displacement $\psi(x,y)$. The displacements are assumed to be

$$u_x=\frac{\partial\psi(x,y)}{\partial x},\quad u_y=\frac{\partial\psi(x,y)}{\partial y} \tag{20}$$

which give the strains

$$\varepsilon_{xx}=\frac{\partial^2\psi(x,y)}{\partial x^2},\quad \varepsilon_{yy}=\frac{\partial^2\psi(x,y)}{\partial y^2},\quad \varepsilon_{xy}=\frac{\partial^2\psi(x,y)}{\partial x\partial y} \tag{21}$$

The constitutive equations are

$$\sigma_{xx}=\frac{E_0\nu_0}{(1+\nu_0)(1-2\nu_0)}(\varepsilon_x+\varepsilon_y)+\frac{E_0}{1+\nu_0}\varepsilon_{xx}-\frac{\beta_0E_0}{1-2\nu_0}\theta_0$$

$$\sigma_{yy}=\frac{E_0\nu_0}{(1+\nu_0)(1-2\nu_0)}(\varepsilon_x+\varepsilon_y)+\frac{E_0}{1+\nu_0}\varepsilon_{yy}-\frac{\beta_0E_0}{1-2\nu_0}\theta_0$$

$$\sigma_{xy}=\frac{E_0}{1+\nu_0}\varepsilon_{xy} \tag{22}$$

where E_0, ν_0, and β_0 are the Young's modulus, Poisson's ratio, and the CTE of the PMMA, respectively. The equilibrium equations require

$$\frac{\partial^2\psi(x,y)}{\partial y^2}+\frac{\partial^2\psi(x,y)}{\partial x^2}=\frac{1+\nu_0}{1-\nu_0}\beta_0\theta_0 \tag{23}$$

The solution of the preceding equation is given by

$$\psi(x,y)=\frac{1}{2\pi}\frac{1+\nu_0}{1-\nu_0}\beta_0\int_{\xi=-\infty}^{\infty}\int_{\eta=-h_0}^{0}\theta_0(\xi,\eta)\times\ln\sqrt{(x-\xi)^2+(y-\eta)^2}\,d\xi d\eta \tag{24}$$

The displacements can then be obtained by Eq. (20) as

$$u_x=\frac{1}{2\pi}\frac{1+\nu_0}{1-\nu_0}\beta_0\int_{\xi=-\infty}^{\infty}\int_{\eta=-h_0}^{0}\theta_0(\xi,\eta)\frac{x-\xi}{(x-\xi)^2+(y-\eta)^2}d\xi d\eta$$

$$u_y=\frac{1}{2\pi}\frac{1+\nu_0}{1-\nu_0}\beta_0\int_{\xi=-\infty}^{\infty}\int_{\eta=-h_0}^{0}\theta_0(\xi,\eta)\frac{y-\eta}{(x-\xi)^2+(y-\eta)^2}d\xi d\eta \tag{25}$$

The displacements at $y=0$ are given by

$$u_x^0=\frac{1}{2\pi}\frac{1+\nu_0}{1-\nu_0}\beta_0\int_{\xi=-\infty}^{\infty}\int_{\eta=-h_0}^{0}\theta_0(\xi,\eta)\frac{x-\xi}{(x-\xi)^2+\eta^2}d\xi d\eta$$

$$u_y^0=\frac{1}{2\pi}\frac{1+\nu_0}{1-\nu_0}\beta_0\int_{\xi=-\infty}^{\infty}\int_{\eta=-h_0}^{0}\theta_0(\xi,\eta)\frac{-\eta}{(x-\xi)^2+\eta^2}d\xi d\eta \tag{26}$$

The combination of Eqs. (21)–(23) gives the stresses

$$\sigma_{xx}=-\frac{E_0}{1+\nu_0}\frac{\partial^2\psi}{\partial y^2},\quad \sigma_{yy}=-\frac{E_0}{1+\nu_0}\frac{\partial^2\psi}{\partial x^2},\quad \sigma_{xy}=\frac{E_0}{1+\nu_0}\frac{\partial^2\psi}{\partial x\partial y} \tag{27}$$

The tractions at $y=-h_0$ are

$$\sigma_{yy}^{h_0} = -\frac{E_0\beta_0}{2\pi(1-\nu_0)}\int_{\xi=-\infty}^{\infty}\int_{\eta=-h_0}^{0}\theta_0(\xi,\eta)\frac{(h_0+\eta)^2-(x-\xi)^2}{\left[(x-\xi)^2+(h_0+\eta)^2\right]^2}\times d\xi d\eta$$

$$\sigma_{xy}^{h_0} = -\frac{E_0\beta_0}{2\pi(1-\nu_0)}\int_{\xi=-\infty}^{\infty}\int_{\eta=-h_0}^{0}\theta_0(\xi,\eta)\frac{-2(x-\xi)(h_0+\eta)}{\left[(x-\xi)^2+(h_0+\eta)^2\right]^2}\times d\xi d\eta \tag{28}$$

3.2 Solutions for Auxiliary Problem II. The Airy stress function for this problem can be written as [17]

$$\phi(x,y) = \frac{2}{\pi}\int_0^{\infty}\bar{\phi}(\xi,y)\cos(\xi x)d\xi \tag{29}$$

Substituting the preceding equations into the biharmonic equation and solving for ϕ, one can obtain

$$\phi(x,y) = \frac{2}{\pi}\int_0^{\infty}\left\{[A(\xi)+yB(\xi)]e^{-\xi y}+[C(\xi)+yD(\xi)]e^{\xi y}\right\}\times\cos(\xi x)d\xi \tag{30}$$

where $A(\xi)$, $B(\xi)$, $C(\xi)$, and $D(\xi)$ are to be determined from the boundary conditions. The stress components are given by

$$\sigma_{xx} = \frac{\partial^2\phi}{\partial y^2} = \frac{2}{\pi}\int_0^{\infty}\left[\xi^2e^{-\xi y}A+\left(\xi^2y-2\xi\right)e^{-\xi y}B+\xi^2e^{\xi y}C+\left(\xi^2y+2\xi\right)e^{\xi y}D\right]\cos(\xi x)d\xi$$

$$\sigma_{yy} = \frac{\partial^2\phi}{\partial x^2} = -\frac{2}{\pi}\int_0^{\infty}\left(\xi^2e^{-\xi y}A+\xi^2ye^{-\xi y}B+\xi^2e^{\xi y}C+\xi^2ye^{\xi y}D\right)\times\cos(\xi x)d\xi$$

$$\sigma_{xy} = -\frac{\partial^2\phi}{\partial x\partial y} = \frac{2}{\pi}\int_0^{\infty}\left[-\xi e^{-\xi y}A+(1-\xi y)e^{-\xi y}B+\xi e^{\xi y}C+(1+\xi y)e^{\xi y}D\right]\xi\sin(\xi x)d\xi \tag{31}$$

From the plane-strain constitutive equations, the displacements can be solved as

$$u_x(x,y) = \frac{2}{\pi}\frac{1+\nu_0}{E_0}\int_0^{\infty}\left[\xi e^{-\xi y}A+(-2+2\nu_0+\xi y)e^{-\xi y}B+\xi e^{\xi y}C+(2-2\nu_0+\xi y)e^{\xi y}D\right]\sin(\xi x)d\xi$$

$$u_y(x,y) = \frac{2}{\pi}\frac{1+\nu_0}{E_0}\int_0^{\infty}\left[\xi e^{-\xi y}A+(\xi y+1-2\nu_0)e^{-\xi y}B-\xi e^{\xi y}C-(\xi y-1+2\nu_0)e^{\xi y}D\right]\cos(\xi x)d\xi \tag{32}$$

The boundary conditions $\sigma_{yy} = -\sigma_{yy}^{h_0}$ and $\sigma_{xy} = -\sigma_{xy}^{h_0}$ at $y = -h_0$ and $u_x = -u_x^0$ and $u_y = -u_y^0$ at $y = 0$ yield the following equations:

$$\begin{bmatrix} -\xi^2e^{\xi h_0} & \xi^2h_0e^{\xi h_0} & -\xi^2e^{-\xi h_0} & \xi^2h_0e^{-\xi h_0} \\ -\xi^2e^{\xi h_0} & (\xi+\xi^2h_0)e^{\xi h_0} & \xi^2e^{-\xi h_0} & (\xi-\xi^2h_0)e^{-\xi h_0} \\ \xi & -2+2\nu_0 & \xi & 2-2\nu_0 \\ \xi & 1-2\nu_0 & -\xi & 1-2\nu_0 \end{bmatrix}\begin{Bmatrix} A \\ B \\ C \\ D \end{Bmatrix} = -\begin{Bmatrix} \int_{x=0}^{\infty}\sigma_{yy}^{h_0}\cos(\xi x)dx \\ \int_{x=0}^{\infty}\sigma_{yy}^{h_0}\sin(\xi x)dx \\ \int_{x=0}^{\infty}\frac{E_0}{1+\nu_0}u_x^0\sin(\xi x)dx \\ \int_{x=0}^{\infty}\frac{E_0}{1+\nu_0}u_y^0\cos(\xi x)dx \end{Bmatrix} \tag{33}$$

which are used to solve A, B, C, and D. The superposition of Problem I and Problem II gives the vertical displacement at the PMMA top surface as

$$u_y^{\text{surface}}(x) = -\frac{1}{2\pi}\frac{1+\nu_0}{1-\nu_0}\beta_0\int_{\xi=-\infty}^{\infty}\int_{\eta=-h_0}^{0}\theta_0(\xi,\eta)\times\frac{h_0+\eta}{(x-\xi)^2+(h_0+\eta)^2}d\xi d\eta+\frac{2(1+\nu_0)}{\pi E_0}\times\int_0^{\infty}\left[\xi e^{\xi h_0}A+(-\xi h_0+1-2\nu_0)e^{\xi h_0}B-\xi e^{-\xi h_0}C-(-\xi h_0-1+2\nu_0)e^{-\xi h_0}D\right]\cos(\xi x)d\xi \tag{34}$$

and its amplitude is $|u_y^{\text{surface}}(x)|$, which is the detected thermal expansion in the experiment.

4 Scaling Law for Thermal Expansion

The temperature increase and thermal expansion in Secs. 2 and 3 are very complex. In this section, we will establish a simple scaling law to clearly show the influences of various material, geometric, and loading parameters (e.g., power per unit length Q_0). Such a scaling law is very useful to map the thermal expansion to the temperature distribution and determine Q_0.

The thermal diffusion length is defined as $L_0 = 1/q_0 = \sqrt{\alpha_0/(2\omega)} = \sqrt{\alpha_0/(4\pi f)}$. The thermal diffusivity of PMMA is $\sim 10^{-7}$ m^2 s^{-1}, such that L_0 is larger than, or on the order of, 1 μm for a frequency smaller than 100 kHz [18]. In experiments, the PMMA thickness (h_0) is usually on the order of 100 nm, which is much smaller than the thermal diffusion length. Therefore, the temperature throughout the thickness of the PMMA can be approximately equal to its surface temperature in Eq. (19), which can be rewritten by changing $\eta = sr$ as

$$\theta_{\text{surface}}(x)=\frac{2Q_0}{\pi^2 k_1}\int_0^\infty \left\langle \begin{matrix} \left\{\frac{1-\kappa}{1+\kappa}\cosh\left[\frac{h_0}{r}\sqrt{\eta^2+\mathrm{i}(q_0 r)^2}\right]+\frac{k_0\sqrt{\eta^2+\mathrm{i}(q_0 r)^2}}{k_1\sqrt{\eta^2+\mathrm{i}(q_1 r)^2}}\sinh\left[\frac{h_0}{r}\sqrt{\eta^2+\mathrm{i}(q_0 r)^2}\right]\right\}^{-1} \\ \frac{\sin\left(\frac{\pi}{2}\eta\right)}{\eta\sqrt{\eta^2+\mathrm{i}(q_1 r)^2}}\cos\left(\frac{x}{r}\eta\right) \end{matrix} \right\rangle d\eta \tag{35}$$

where

$$\kappa=\frac{1-\frac{k_2}{k_1}\frac{\sqrt{\eta^2+\mathrm{i}(q_2 r)^2}}{\sqrt{\eta^2+\mathrm{i}(q_1 r)^2}}}{1+\frac{k_2}{k_1}\frac{\sqrt{\eta^2+\mathrm{i}(q_2 r)^2}}{\sqrt{\eta^2+i(q_1 r)^2}}}e^{-2\frac{h_1}{r}\sqrt{\eta^2+\mathrm{i}(q_1 r)^2}}$$

The thermal conductivity and diffusivity are $k_0=0.19\ \mathrm{Wm^{-1}K^{-1}}$ and $\alpha_0=1.1\times10^{-7}\ \mathrm{m^2s^{-1}}$ for PMMA [18,19], $k_1=1.3\ \mathrm{Wm^{-1}K^{-1}}$ and $\alpha_1=8.4\times10^{-7}\ \mathrm{m^2s^{-1}}$ for SiO_2 [20], and $k_2=120\ \mathrm{Wm^{-1}K^{-1}}$ and $\alpha_2=7.3\times10^{-5}\ \mathrm{m^2s^{-1}}$ for Si [21], respectively. The thicknesses of the PMMA and SiO_2 are on the order of 100 nm. The integrand in Eq. (35) rapidly decreases within a range of 10^{-2} and, therefore, $\sin((\pi/2)\eta)\approx(\pi/2)\eta$. For frequencies smaller than 100 kHz and SWNT radius $r\sim1$ nm, $q_0 r$, $q_1 r$, and $q_2 r$ are smaller than, or on the order of, 10^{-3} such that they can be neglected. These, together with a large ratio $k_2/k_1\sim100$ and a small ratio $k_0/k_1\sim0.1$, simplify Eq. (35) to

$$\theta_{\text{surface}}(x)=\frac{Q_0}{\pi k_1}g\left(\frac{x}{r};\frac{h_0}{r},\frac{h_1}{r}\right) \tag{36}$$

where

$$g\left(\frac{x}{r};\frac{h_0}{r},\frac{h_1}{r}\right)=\int_0^\infty\frac{\tanh\left(\frac{h_1}{r}\eta\right)\cos\left(\frac{x}{r}\eta\right)}{\eta\cosh\left(\frac{h_0}{r}\eta\right)}d\eta \tag{37}$$

is a nondimensional function of the normalized position x/r. It depends only on the normalized thicknesses h_0/r and h_1/r, which will be studied in Sec. 5.

Since the temperature in the PMMA is independent of its thickness, which is very thin, we can further assume that the plane stress is valid in the y direction, i.e., $\sigma_{yy}=0$ and $\sigma_{xy}=0$. The amplitude of the oscillating vertical displacement of the PMMA can be obtained as

$$\begin{aligned}u_y^{\text{surface}}(x)&=\frac{1+\nu_0}{1-\nu_0}\beta_0 h_0\theta_{\text{surface}}(x)\\&=Q_0\frac{(1+\nu_0)\beta_0 h_0}{(1-\nu_0)\pi k_1}g\left(\frac{x}{r};\frac{h_0}{r},\frac{h_1}{r}\right)\end{aligned} \tag{38}$$

This simple expression shows that the temperature distribution has the same profile as the thermal expansion but a different amplitude with a factor of $(1+\nu_0/1-\nu_0)\beta_0 h_0$. With all other materials and geometric parameters known, the power dissipation per unit length Q_0 can be easily determined.

5 Results and Discussion

An FEA is also performed to validate the analytical models. A 2D model is developed using the commercial software (COMSOL) with the combined modules of heat conduction (transient) and mechanical stress-strain analysis (quasi-static). The width of the simulated domain is 200 μm. The Si substrate has a finite thickness of 500 μm. The heat source $Q(t)=Q_0[1+\cos(2\omega t)]$ is applied to the SWNT at the interface between the PMMA and SiO_2. The bottom of the Si is set to a constant temperature and all of the other surfaces have natural convection with the coefficient of heat convection of $25\ \mathrm{Wm^{-2}K^{-1}}$. The mechanics boundaries include fully constrained at the bottom of the Si substrate and traction-free boundaries at the other surfaces. The thermal properties of the PMMA, SiO_2, and Si are given in Sec. 4. The CTE, Young's modulus, and Poisson's ratio are $\beta_0=50\times10^{-6}\ \mathrm{K^{-1}}$, $E_0=3.0$ GPa, and $\nu_0=0.35$ for the PMMA [16,22,23], $\beta_1=0.5\times10^{-6}\ \mathrm{K^{-1}}$, $E_1=64$ GPa, and $\nu_1=0.17$ for the SiO_2 [14,24,25], and $\beta_2=2.6\times10^{-6}\ \mathrm{K^{-1}}$, $E_2=165$ GPa, and $\nu_2=0.28$ for the SiO_2 [15,24,26]. The amplitude of the out-of-plane thermal expansion at the top surface is extracted from the final cycle of the simulation to ensure the results to be steady state.

Figure 4 compares the distribution of the approximate surface temperature increase in Eq. (36) to the FEA and the accurate surface temperature increase in Eq. (35) for the power dissipation per unit length $Q_0=1$ W/m at $f=30$ kHz. The thicknesses are $h_0=26$ nm for the PMMA and $h_1=90$ nm for the SiO_2. The radius of the SWNT is $r=1$nm. The results clearly show that the simple expression of temperature increase agrees well with the FEA and the complex accurate solution. The thermal expansion profiles along the cross section are shown in Fig. 5. The power dissipation per unit length Q_0 is determined to be $7.7\ \mathrm{Wm^{-1}}$. It is observed that the simple expression of thermal expansion in Eq. (38) gives a good approximation.

The achievable level of spatial resolution is an important characteristic of the SJEM measurement. This level is fully determined by the nondimensional function $g(x/r;h_0/r,h_1/r)$. The characteristic width is defined as the full width at half-maximum (FWHM), which can be solved for x/r in $g(x/r;h_0/r,h_1/r)=(1/2)g(0;h_0/r,h_1/r)$, i.e.,

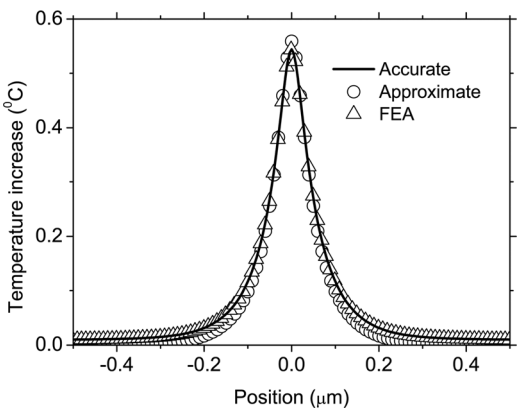

Fig. 4 Surface temperature distribution along the cross sections given by the analytical model of the accurate and approximate solutions and the FEA for the power density $Q_0=1$ W/m at $f=30$ kHz

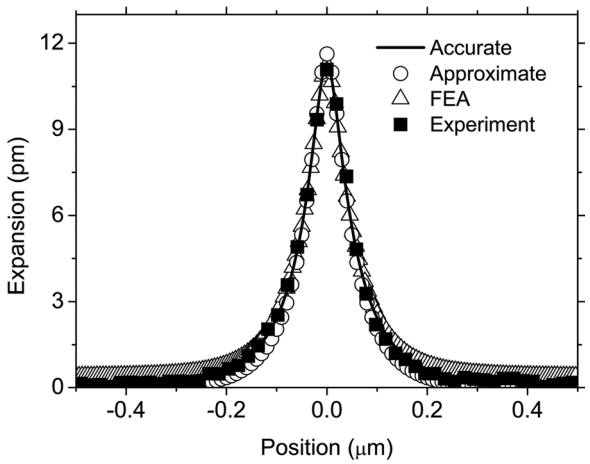

Fig. 5 Expansion profiles along the cross sections given by the analytical model of the accurate and approximate solutions and the FEA with the power density determined as $Q_0 = 7.7$ W/m at $f = 30$ kHz

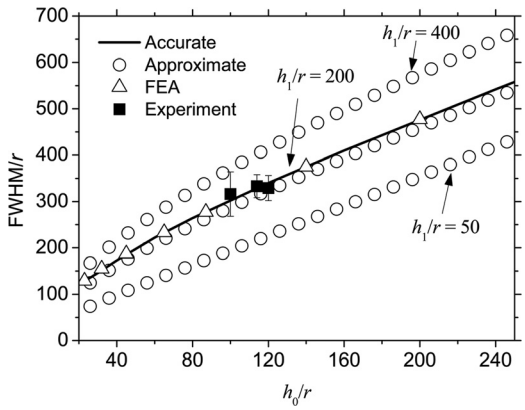

Fig. 6 The normalized FWHM (FWHM/r) versus the normalized PMMA thickness (h_0/r) at different normalized SiO_2 thicknesses (h_1/r)

$$\int_0^\infty \frac{\tanh\left(\frac{h_1}{r}\eta\right)}{\eta\cosh\left(\frac{h_0}{r}\eta\right)}\left[\cos\left(\frac{x}{r}\eta\right)-\frac{1}{2}\right]d\eta = 0 \tag{39}$$

Figure 6 shows the normalized FWHM by r versus the normalized PMMA thickness (h_0/r) at different normalized SiO_2 thicknesses (h_1/r). The good agreement among the accurate solution, approximate solution, the FEA, and experiments [11] at $h_1/r = 200$ validates the models. The FWHM increases almost linearly with the thickness of the PMMA, corresponding to the decrease in spatial resolution. As the thickness of SiO_2 increases, the FWHM also increases. These results suggest that thin PMMA and thin SiO_2 give a high resolution. For $h_0/r \sim 10$ and $h_1/r \sim 10$, the spatial resolution is as good as ~50 nm.

6 Concluding Remarks

We have developed an analytical model to study the thermal imaging of single-walled carbon nanotube devices by SJEM. The analytical model is validated by finite element simulations and experiments. A simple scaling law at low frequencies (<100 kHz) for thermal expansion in terms of the material and geometrical parameters is obtained. The normalized thermal expansion only depends on two nondimensional geometric parameters: the normalized PMMA thickness and the normalized SiO_2 thickness. Such a scaling law provides a simple way to determine the surface temperature distribution from the measured thermal expansion in experiments. With other material and geometrical parameters known, the only free parameter power dissipation per unit length in an SWNT can be determined. The results suggest the thinner the PMMA and SiO_2 layers, the higher the spatial resolution, which is as good as ~50 nm.

Acknowledgment

J.S. acknowledges the support from the Provost Award from the University of Miami. C.L. acknowledges the support from the NSFC (Grant No. 11172263).

References

[1] Avouris, P., Chen, Z. H., and Perebeinos, V., 2007, "Carbon-Based Electronics," Nat. Nanotechnol., **2**, pp. 605–615.
[2] Franklin, A. D., Luisier, M., Han, S. J., Tulevski, G., Breslin, C. M., Gignac, L., Lundstrom, M. S., and Haensch, W., 2012, "Sub-10 nm Carbon Nanotube Transistor," Nano Lett., **12**, pp. 758–762.
[3] Robertson, J., 2007, "Growth of Nanotubes for Electronics," Mater. Today, **10**, pp. 36–43.
[4] Shi, L., Plyasunov, S., Bachtold, A., McEuen, P. L., Majumdar, A., 2000, "Scanning Thermal Microscopy of Carbon Nanotubes Using Batch-Fabricated Probes," Appl. Phys. Lett., **77**, pp. 4295–4297.
[5] Small, J. P., Shi, L., and Kim, P., 2003, "Mesoscopic Thermal and Thermoelectric Measurements of Individual Carbon Nanotubes," Solid State Commun., **127**, pp. 181–186.
[6] Jo, I., Hsu, I. K., Lee, Y. J., Sadeghi, M. M., Kim, S., Cronin, S., Tutuc, E., Banerjee, S. K., Yao, Z., and Shi, L., 2011, "Low-Frequency Acoustic Phonon Temperature Distribution in Electrically Biased Graphene," Nano Lett., **11**, pp. 85–90.
[7] Yu, Y. J., Han, M. Y., Berciaud, S., Georgescu, A. B., Heinz, T. F., Brus, L. E., Kim, K. S., and Kim, P., 2011, "High-Resolution Spatial Mapping of the Temperature Distribution of a Joule Self-Heated Graphene Nanoribbon," Appl. Phys. Lett., **99**, p. 183105.
[8] McConney, M. E., Kulkarni, D. D., Jiang, H., Bunning, T. J., and Tsukruk, V. V., 2012, "A New Twist on Scanning Thermal Microscopy," Nano Lett., **12**, pp. 1218–1223.
[9] Varesi, J., and Majumdar, A., 1998, "Scanning Joule Expansion Microscopy at Nanometer Scales," Appl. Phys. Lett., **72**, pp. 37–39.
[10] Majumdar, A., and Varesi, J., 1998, "Nanoscale Temperature Distributions Measured by Scanning Joule Expansion Microscopy," ASME Trans. J. Heat Transfer., **120**, pp. 297–305.
[11] Xie, X., Grosse, K. L., Song, J., Lu, C., Dunham, S., Du, F., Islam, A. E., Li, Y., Zhang, Y., Pop, E., Huang, Y., King, W. P., and Rogers, J. A., 2012, "Quantitative Thermal Imaging of Single-Walled Carbon Nanotube Devices by Scanning Joule Expansion Microscopy," ACS Nano, **6**, pp. 10267–10275.
[12] Gurrum, S. J., Joshi, Y. K., King, W. P., and Ramakrishna, K., 2005, "Scanning Joule Expansion Microscopy of a Constriction in a Thin Metallic Film," ASME J. Heat Transfer, **127**, p. 809.
[13] Grosse, K. L., Bae, M. H., Lian, F., Pop, E., and King, W. P., 2011, "Nanoscale Joule Heating, Peltier Cooling and Current Crowding in Graphene-Metal Contacts," Nat. Nanotechnol., **6**, pp. 287–290.
[14] Blech, I., and Cohen, U., 1982, "Effects of Humidity on Stress in Thin Silicon Dioxide Films," J. Appl. Phys., **53**, pp. 4202–4207.
[15] Okada, Y., and Tokumaru, Y., 1984, "Precise Determination of Lattice-Parameter and Thermal-Expansion Coefficient of Silicon Between 300 K and 1500 K," J. Appl. Phys., **56**, pp. 314–320.
[16] Chou, S. Y., and Krauss, P. R., 1997, "Imprint Lithography With Sub-10 nm Feature Size and High Throughput," Microelectron. Eng., **35**, pp. 237–240.
[17] Civelek, M. B., 1985, "Stress Intensity Factors for System of Cracks in an Infinite Strip," Fracture Mechanics: Sixteenth Symposium, ASTM Spec. Tech. Publ., **868**, pp. 7–26.
[18] Tsutsumi, N., and Kiyotsukuri, T., 1988, "Measurement of Thermal-Diffusivity for Polymer Film by Flash Radiometry," Appl. Phys. Lett., **52**, pp. 442–444.
[19] Assael, M. J., Botsios, S., Gialou, K., and Metaxa, I. N., 2005, "Thermal Conductivity of Polymethyl Methacrylate (PMMA) and Borosilicate Crown Glass BK7," Int. J. Thermophys., **26**, pp. 1595–1605.
[20] Ju, Y. S., and Goodson, K. E., 1999, "Process-Dependent Thermal Transport Properties of Silicon-Dioxide Films Deposited Using Low-Pressure Chemical Vapor Deposition," J. Appl. Phys., **85**, pp. 7130–7134.
[21] Liu, W. J., Etessam-Yazdani, K., Hussin, R., and Asheghi, M., 2006, "Modeling and Data for Thermal Conductivity of Ultrathin Single-Crystal SOI

Layers at High Temperature," IEEE Trans. Electron Devices, **53**, pp. 1868–1876.
[22] Ishiyama, C., and Higo, Y., 2002, "Effects of Humidity on Young's Modulus in Poly(Methyl Methacrylate)," J. Polym. Sci., Part B: Polym. Phys., **40**, pp. 460–465.
[23] Wu, W. L., Vanzanten, J. H., Orts, W. J., 1995, "Film Thickness Dependent Thermal-Expansion in Ultrathin Poly(Methyl Methacrylate) Films on Silicon," Macromolecules, **28**, pp. 771–774.
[24] Tada, H., Kumpel, A. E., Lathrop, R. E., Slanina, J. B., Nieva, P., Zavracky, P., Miaoulis, I. N., and Wong, P. Y., 2000, "Thermal Expansion Coefficient of Polycrystalline Silicon and Silicon Dioxide Thin Films at High Temperatures," J. Appl. Phys., **87**, pp. 4189–4193.
[25] Kim, M. T., 1996, "Influence of Substrates on the Elastic Reaction of Films for the Microindentation Tests," Thin Solid Films, **283**, pp. 12–16.
[26] Wortman, J. J., and Evans, R. A., 1956, "Young's Modulus, Shear Modulus and Poisson's Ratio in Silicon and Germanium," J. Appl. Phys., **36**, p. 153.